Memoirs of the Faculty of Engineering, Nagoya University
Vol. 37, No. 2 (1985) — Research Report —

TURBULENT TRANSONIC FLOW FOR NACA 0012 / RAE 2822 AIRFOILS UNDER BALDWIN-LOMAX MODEL

TOSHI FUJIWARA, YI-YUN WANG and YASUNORI OHMORI

Department of Aeronautical Engineering

(Received Octover 31, 1985)

Abstract

The Beam-Warming scheme was applied to transonic flows around two-dimensional airfoils NACA 0012 and RAE 2822, taking account of the Baldwin-Lomax turbulence model. After appropriate grid generation techniques, the calculation successfully lead to steady flows containing a shock wave and flow separation, for a uniform flow Mach number 0.75, the Reynolds number 6×10^6, and angles of attack 0 to 15 degrees. Note that periodical oscillations were observed at high angles of attack.

1. Introduction

In the previous works [1, 2], both Euler and Navier-Stokes equations were solved for a two-dimensional symmetrical airfoil NACA 0012 under laminar flow conditions. Although a shock wave was formed in an inviscid flow at a free stream Mach number $M_\infty=0.75$ and and angle of attack $\alpha=2$ degrees utilizing Euler equations, Navier-Stokes equations were unsuccessful to gererate a shock wave on the upper surface of the airfoil even at the same Mach number $M_\infty=0.75$ and the angle of attack $\alpha=2$ degrees where $Re=10^4$ or 10^5 assuming laminar flow in the entire flowfield. It is speculated that the reason can be attributed to the low Reynolds numbers and laminar flow conditions, because in a realistic experimental condition the Reynolds number is much higher and as a result the flow would be always turbulent.

In the present paper, therefore, the Reynolds number was raised up to an experimental value 6×10^6 and at the same time the effect of turbulence was introduced by taking account of the Baldwin-Lomax turbulence model [3]. Thus it is expected to successfully produce a shock wave on the upper surface of the

airfoil, along with other interesting phenomena typically like flow separation, vortex generation and oscillation of flowfield. The calculated results will be compared with the existing experimental data [8] on the pressure distribution over the same airfoil surface under the same flow conditions.

We used a single-step scheme which was introduced by Beam and Warming [4] and was successfully applied to numerous transonic flow problems thereafter. Although simpler and essentially more advanced numerical schemes have emerged and been occasionally used recently [5, for example], we still wanted to use one of the most dependable schemes already extensively tested.

2. Numerical Scheme

The single-step scheme introduced by Beam-Warming [4] is shown as

$$\Delta\hat{U}^n=\frac{\theta\Delta\tau}{1+\delta}\frac{\partial}{\partial\tau}\Delta\hat{U}^n+\frac{\Delta\tau}{1+\delta}\frac{\partial}{\partial\tau}\hat{U}^n+\frac{\delta}{1+\delta}\Delta\hat{U}^{n-1}$$

$$+0\left[\left(\theta-\frac{1}{2}-\delta\right)\Delta\tau^2+\Delta\tau^3\right] \tag{1}$$

where $\hat{U}^n=U(n\Delta\tau)$ and $\Delta\hat{U}^n=\hat{U}^{n+1}-\hat{U}^n$. The parameters θ and δ may have various combinations, each resulting in an explicit or implicit, and first-order- or second-order-accurate scheme. The schemes are implicit if $\theta>0$ while they are three-level ones when $\delta>0$. Recently, an implicit and first-order-accurate two-level scheme ($\theta=1$ and $\delta=0$) is called the Euler implicit one [6]. In this paper, an implicit and second-order-accurate three-level scheme ($\theta=1$ and $\delta=1/2$) is applied to solve the full Navier-Strokes equations. Several typical examples have been calculated for subsonic and transonic as well as laminar and turbulent, steady and unsteady flows around NACA 0012 and RAE 2822 airfoils.

1) Grid generation:

Using a transformation based on the solution of the Poisson equations [7], an irregular domain outside an airfoil in the physical plane (x, y) was transformed onto a rectangular one in the computational plane (ξ, η). The airfoil contour is transformed into a part of coordinate line $\eta(x, y)=0$. Another part is a specified cut extending from the trailing edge of the airfoil to the downstream of the flowfield.

Since we are calculating a viscous flow containing extremely thin boundary layers both on the airfoil surface and in the free shear layer, we need to use a grid system adequately clustered in the vicinity of the airfoil and wake. It is noteworthy that the utilized grid system is generated [7] by controlling the distances from $\eta(x, y)=\Delta\eta$ to $\eta(x, y)=0$ and the orthogonalities between all lines of constant ξ and $\eta(x, y)=0$. A typical example of such coarse grids utilized for the NACA 0012 airfoil is illustrated in Fig. 1.

2) Implicit difference scheme:

By means of linearization, spatial factorization and the algorithm shown in Eq. (1), the Navier-Strokes equations are transformed into the following forms in the

(ξ, η) coordinate system:

$$\left\{I+\frac{\theta\Delta\tau}{1+\delta}\left[\frac{\partial}{\partial\xi}\left(\hat{A}-\frac{\hat{P}-\hat{Q}_\xi}{Re}\right)^n-\frac{1}{Re}\frac{\partial^2}{\partial\xi^2}\hat{Q}^n\right]-\omega_i J^{-1}\nabla_\xi\Delta_\xi J\right\}$$

$$\left\{I+\frac{\theta\Delta\tau}{1+\delta}\left[\frac{\partial}{\partial\eta}\left(\hat{B}-\frac{\hat{R}-\hat{S}_\eta}{Re}\right)^n-\frac{1}{Re}\frac{\partial^2}{\partial\eta^2}\hat{S}_n\right]-\omega_i J^{-1}\nabla_\eta\Delta_\eta J\right\}\Delta\hat{U}^n=$$

$$\sin\delta\cdot\frac{\theta\Delta\tau}{1+\delta}\frac{1}{Re}(\Delta\hat{V}_2+\Delta\hat{W}_1)^{n-1}+\frac{\Delta\tau}{1+\delta}\left[\frac{\partial}{\partial\xi}\left(-\hat{F}+\frac{\hat{V}_1+\hat{V}_2}{Re}\right)^n\right.$$

$$\left.+\frac{\partial}{\partial\eta}\left(-\hat{G}+\frac{\hat{W}_1+\hat{W}_2}{Re}\right)^n\right]+\frac{\delta}{1+\delta}\Delta\hat{U}^{n-1}-\omega_e J^{-1}[(\nabla_\xi\Delta_\xi)^2+(\nabla_\eta\Delta_\eta)^2]J\hat{U}^n \tag{2}$$

where $\hat{U}=J^{-1}U=J^{-1}\ (\rho,\ \rho u,\ \rho v,\ e)^T$, $J=(x_\xi y_\eta-x_\eta y_\xi)^{-1}$ and $\hat{F}$, $\hat{V}_1$, $\hat{V}_2$, $\hat{G}$, $\hat{W}_1$ and $\hat{W}_2$ are the flux vectors while $\hat{A}$, $(\hat{P}-\hat{Q}_\xi)$, $\hat{Q}$, $\hat{B}$, $(\hat{R}-\hat{S}_\eta)$ and $\hat{S}$ are the flux Jacobian matrices, and ω_i and ω_e are the coefficients of added dissipative terms. It is noted that Eq. (2) has the following four characteristics: a) It is implicit (when $\theta=1$) and unconditionally stable; thus we can gradually magnify the time steps starting from the CFL number unity up to an enormously high value about 600, although we have to note that there still are stability limits in the CFL number in actuality for non-linear equations. b) All of the conservation-form flux vectors are linearized with respect to time, and therefore $\Delta\hat{U}$ becomes common unknown quantities. c) The process of advancing the solution forward is time-split. d) It is a three-level algorithm; the cross derivative terms are explicitly replaced by the values of previous time.

When $\omega_i=0$, the stability limit becomes $0<\omega_e<(1+2\delta)/8(1+\delta)$, while for $\omega_i\neq 0$ the limit is extended to $0<\omega_e, \omega_i<(1+2\delta)/4(1+\delta)$, as far as a linear theoretical analysis is concerned. In reality, however, the choice of a concrete ω_e depends on experience. If ω_e is too large, shock waves can not be fully resolved.

3) Spatial and time steps:

The minimum grid size was chosen as 0.8×10^{-5} so that 20 grid points were allocated in the boundary layer. In the case of NACA 0012, the Courant number was increased from unity to 600 which was attempted to reach after 1000 steps using geometric progression.

4) Turbulence model:

The Baldwin-Lomax turbulence model [3] is used to incorporate the influence of turbulence, because high-Reynolds-number flows are being analyzed.

3. Results and Discussions — NACA 0012

Even if the Courant number was initially aimed to increase up to 600 after 1000 steps of calculation, smaller Courant numbers were carefully used when the

stepwise relative change of any dependent variable had exceeded $10^{-3.7}$. Regarding the artificial viscosity, we chose

$$\omega_e = \omega_i = \frac{1+2\delta}{8(1+\delta)} \tag{3}$$

where $\delta = 0.5$.

From now on we are going to show results on the flows around the NACA 0012 symmetrical airfoil in the free stream Mach number $M_\infty = 0.75$ and $Re = 6 \times 10^6$ at various angles of attack.

1) $\alpha = 4$ degrees.

Figs. 2 (a)～(c) show a steady-state flow for the angle of attack $\alpha = 4$ degrees. This steady state was achieved 6000 steps after the start of the calculation, which corresponds to the dimensionless time 35.72. Since the time was nondimensionalized by L(chord length)$/C_\infty$(freestream sound velocity), this number was equal to the time for a disturbance from the airfoil to make 3 round trips in the solution domain of size about $6L$ (from airfoil to the boundary); usually, the time is considered enough to establish a steady flow. As shown in Figs. 2 (a) and (b), the upper surface forms a shock wave from the root of which the boundary layer separation starts. The pressure distributions on both sides of the airfoil in Fig. 2 (c) clearly show the formation of a shock on the upper surface and the net lift due to the pressure differences.

2) $\alpha = 6$ degrees (high angle of attack).

As shown in Figs. 3(i-a) through (iv-c), a high angle of attack produces unsteady flow motions. The unsteadiness is seen in any of the distributions of (a) velocity vectors, (b) equi-Mach-number contours and (c) pressure over the airfoil surface. When the dimensionless time proceeds from 3.2 to 35.0, the point of separation where the velocity profile in the boundary layer starts showing a flow reversal moves back and forth nearly periodically. At $t = 3.2$ the separation point is located close to the middle, moves upstream to the 1/4 chord region at $t = 14.2$, and then further upstream at $t = 24.6$, followed by complete disappearance of the separation point at $t = 35.0$.

The motion of the separation point almost corresponds to the root of a shock wave on the upper surface, as seen in Figs. 3 (i-b), (ii-b), (iii-b) and (iv-b); although the velocity vectors in Fig. 3 (iv-a) do not clearly show flow separation at $t = 35.0$, the equi-Mach number contours indicate the separation point near the 2/3 chord length region. When we observe the pressure distributions over the airfoil surface, seen in Figs. 3 (i-c), (ii-c), (iii-c) and (iv-c), periodical behaviors are most distinctively recognized. It is noted here, however, that the observed unsteady motion does not reflect a truly physical phenomenon, because the utilized Courant number maximum 600 is far beyond the unsteady limit.

3) $\alpha = 15$ degrees (very high angle of attack).

When the angle of attack is increased even further, the tendency of oscillation becomes weaker. As shown in Figs. 4 (a) ～ (c), the flow has separated already in the vicinity of the leading edge where there is not a shock wave but an intense reversed flow forming a large vortex over the entire upper surface. Fig. 4 (a) illustrates, however, that the lift is still high.

4. Results and Discussions — RAE 2822

In order to analyze a flow around a supercritical airfoil RAE 2822, which has conveniently experimental data [8] to compare with calculated results, we slightly changed the choice of parameters. First, the Courant number was attempted to increase from unity to 4000 after 4000 steps of calculation. The actual change of the Courant number was limited at about 300 by the imposed requirement that the stepwise relative variation of dependent variables had to be less than $10^{-3.7}$ to avoid numerical divergence. In other words, the Courant number reached about 300 at 18000 steps which corresponded to dimensionless time 26.7.

Second, the artificial viscosity was gradually decreased from $\sigma_\omega=20$ to 2 during 4000 steps of calculation, where $\omega_e=\omega_i=\sigma_\omega \Delta\tau$.

1) Calculation using Grid 1.

The grid system we use at first is called Grid 1, shown in Fig. 5 (a). Although this grid is orthogonal in the boundary layer region surrounding the airfoil, as clearly seen in the detailed view of the grid, Fig. 5 (b), the orthogonality does not hold in the upper, lower and rear boundaries of the solution domain.

At 7000 steps ($t=9.94$), where the calculation was not long enough to attain steadiness, a numerical divergence halted further computation. The results slightly before the are shown in Figs. 5 (c) and (d). The pressure distributions were compared with the experimental data for $M_\infty=0.75$, $Re=6.2\times10^6$ and $\alpha=3.19$ degrees, as shown in Fig. 5 (d). Apparently, the disagreement exists onlynear the leading edge and shock wave, even though the results eventually diverged.

2) Calculation using Grid 2.

Next, we used a grid system called Grid 2, which was an improved version of Grid 1 in terms of orthogonalities near the boundary region of the solution domain, as seen in Figs. 6 (a) and (b). Using a trial and error technique, the minimum grid size in η direction was chosen 1.2×10^{-5} instead of previous 0.8×10^{-5}.

Calculated results are shown in Figs. 6 (c) through (f). This time, due to the revised grid, the solution reached a steady one already at about 6000 steps, as seen in Fig. 6 (f), and showed no change thereafter. In Fig. 6 (f), the temporal behaviors of stepwise relative field variables averaged with respect to the entire domain, e. g. the averaged energy and vertical velocity, were observed to know how the entire field developed with passage of time. Between 4000 and 6000 steps, nearly flat plateau conditions were already realized with sporadic small-amplitude oscillations seen at the level $10^{-3.7}$. Generally speaking, convergence to a steady state was extremely fast when Grid 2 started being utilized. Thus it was concluded that in order to speed up the process of convergence the grid system, in particular in coarse mesh regions, had to be carefully formed, because maximum errors were expected in those regions.

The results at 18000 steps are shown in Figs. 6 (d) and (e). If Fig. 6 (e) is compared with Fig. 5 (d), improvement is conspicuously seen near the leading edge region, although the discrepancy on the shock position has not altered. Comparison between Figs. 5 (c) and 6 (d) shows that the improved calculation provides a

wider supersonic domain, causing sharper leading edge suction.

References

1) Yi-Yun Wang and T. Fujiwara; The Numerical Analysis of Transonic Flow around a Circular Airfoil Using Hybrid Difference Scheme, Memoirs of the Faculty of Engineering, Nagoya University, Vol. 36, No. 1, pp. 68-78, 1984.
2) Yi-Yun Wang and T. Fujiwara; Numerical Analysis of Transonic Flow around a Two-Dimensional Airfoil by Solving Full Navier-Stokes Equations, Memoirs of the Faculty of Engineering, Nagoya University, Vol. 36, No. 2, pp. 138-178, 1984.
3) B. S. Baldwin and H. Lomax; Thin Layer Approximation and Algebraic Model for Separated Turbulent Flows, AIAA Paper 78-257, 1978.
4) R. M. Beam and R. F. Warming; An Implicit Factored Scheme for the Compressible Navier-Stokes Equations, AIAA Journal, Vol. 16, pp. 393-402, 1978.
5) S. Obayashi, K. Katsushima, K. Fujii and K. Kuwahara; Improvements in Efficiency and Reliability for Navier-Stokes Computations Using the LU-ADI Factorization Algorithm, AIAA Paper 86-0338, 1986.
6) J. L. Steger; Implicit Finite-difference Simulation of Flow about Arbitrary Two-Dimensional Geometries, AIAA Journal, Vol. 16, pp. 679-686, 1978.
7) R. L. Sorenson; A Computer Program to Generate Two-Dimensional Grids about Airfoils and Other Shapes by the Use of Poisson's Equations, NASA-TM-81198, May 1980.
8) Experimental Data Base for Computer Program Assessment, AGARD-AR-138, May 1979.

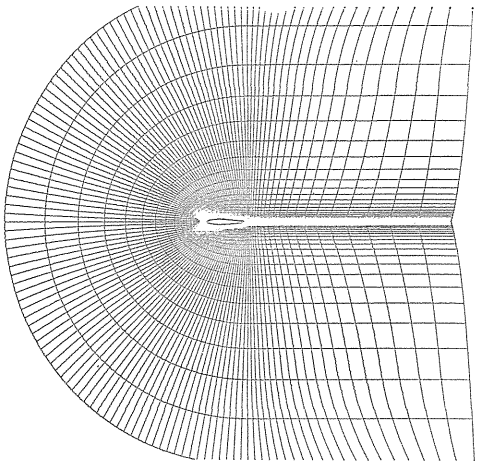

Fig. 1. Grid system used to analyze the NACA 0012 airfoil.

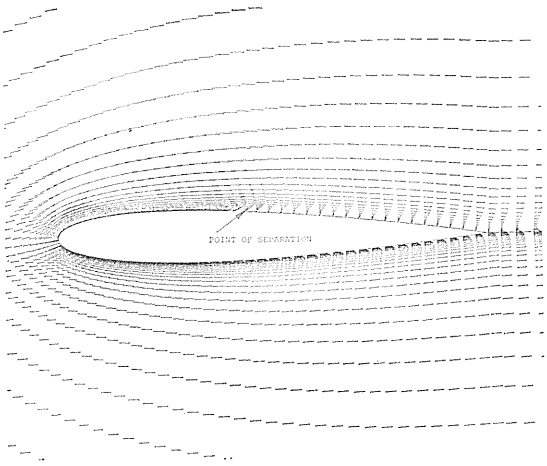

(a) Velocity vector distribution.

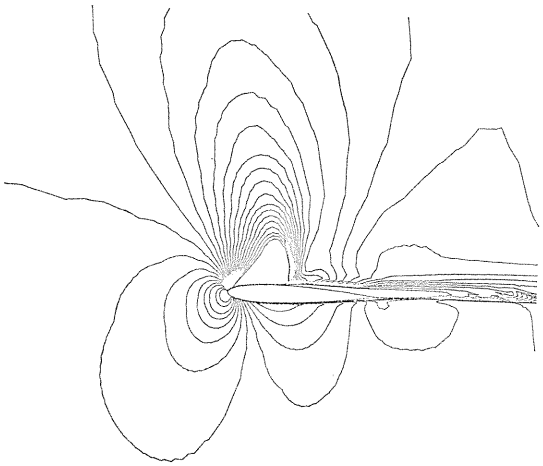

(b) Distribution of equi-Mach-number contours (each contour differs by 0.025).

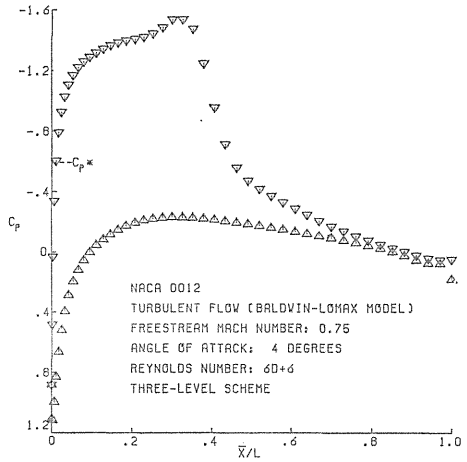

(c) Pressure distribution over the arfoil surface.

Fig. 2. Flow patterns around the NACA 0012 airfoil for $M_\infty=0.75$, $Re=6\times10^6$ and $\alpha=4$ degrees at $N=6000$ steps (dimensionless time $t=35.72$).

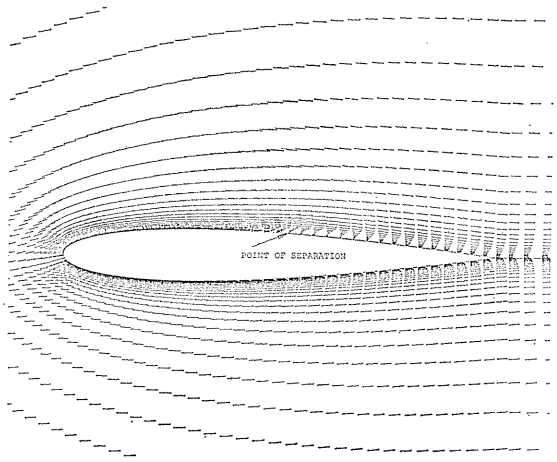

(a) Velocity vector.

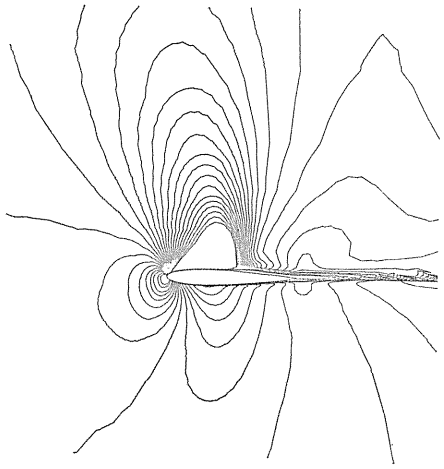

(b) Equi-Mach-number contours.

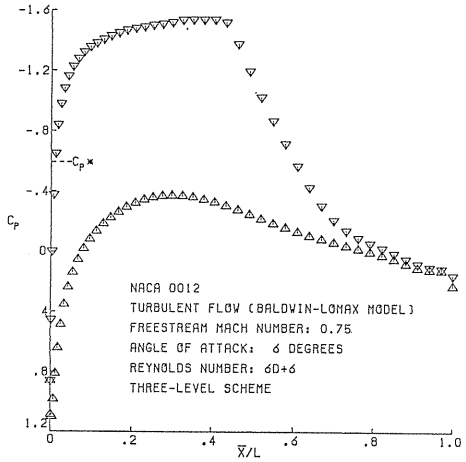

(c) Pressure over the airfoil surface.

Fig. 3. (i) $N=3000$ steps ($t=3.2$)

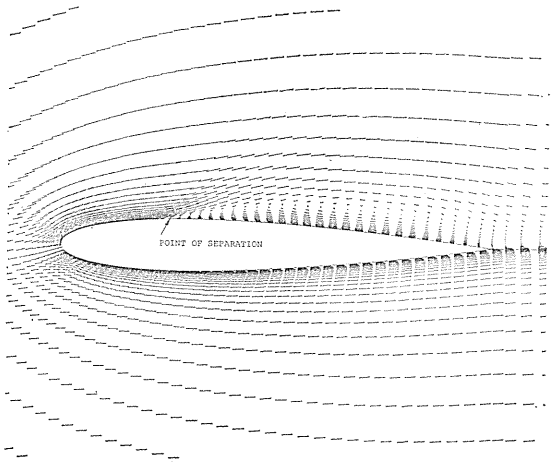

(a) Velocity vector.

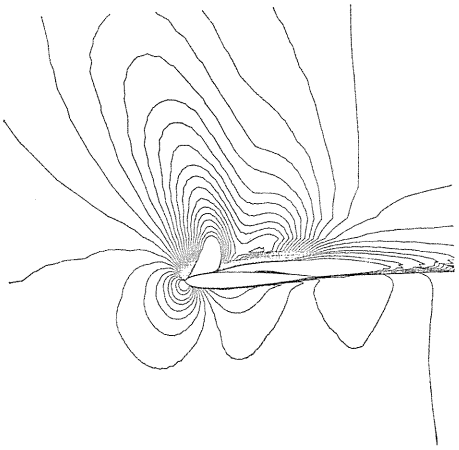

(b) Equi-Mach-number contours.

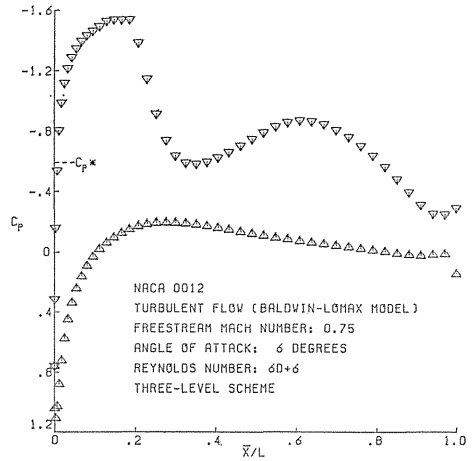

(c) Pressure over the airfoil surface.

Fig. 3. (ii) $N=5000$ steps ($t=14.2$)

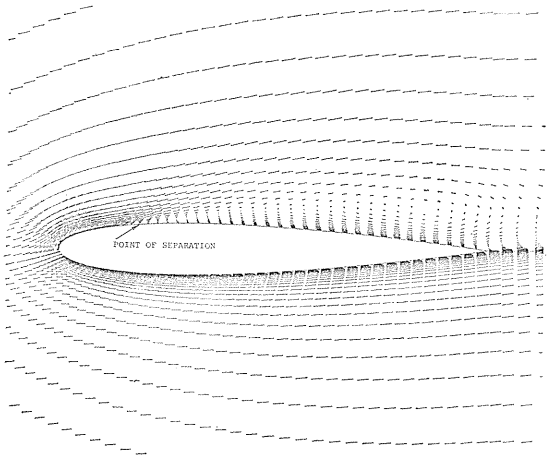

(a) Velocity vector.

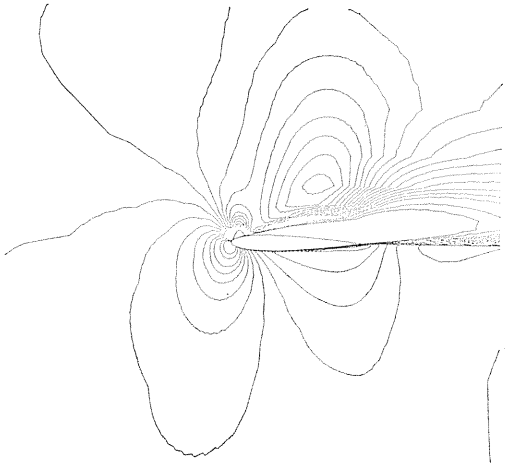

(b) Equi-Mach-number contours.

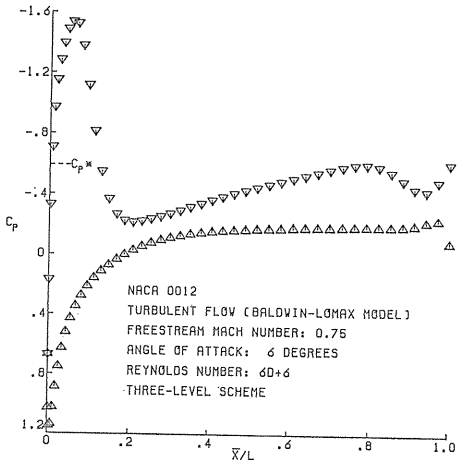

(c) Pressure over the airfoil surface.

Fig. 3. (iii) $N=7000$ steps ($T=24.6$)

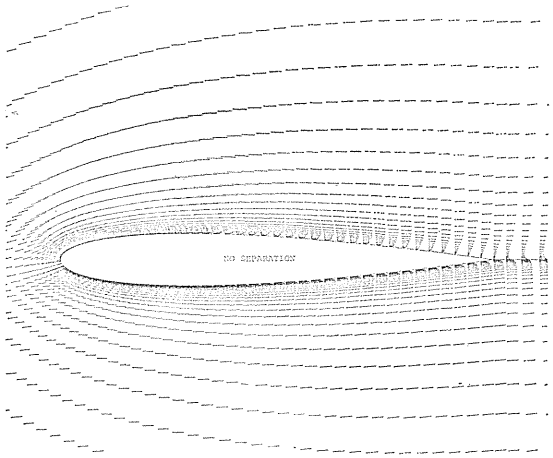

(a) Velocity vector.

(b) Equi-Mach-number contours.

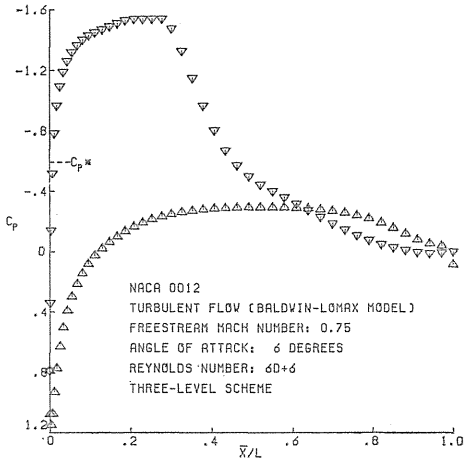

(c) Pressure over the airfoil surface.

(iv) $N=9000$ steps ($t=35.0$)

Fig. 3. NACA 0012 for $M_\infty=0.75$, $Re=6\times10^6$ and $\alpha=6$ degrees.

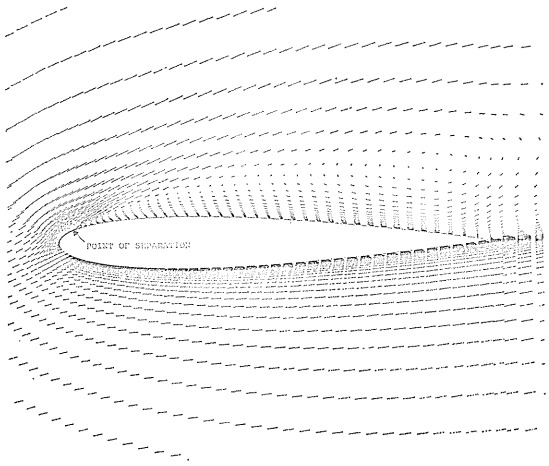

(a) Velocity vector.

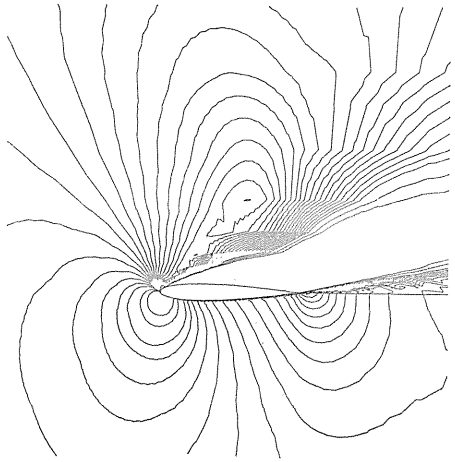

(b) Equi-Mach-number contours.

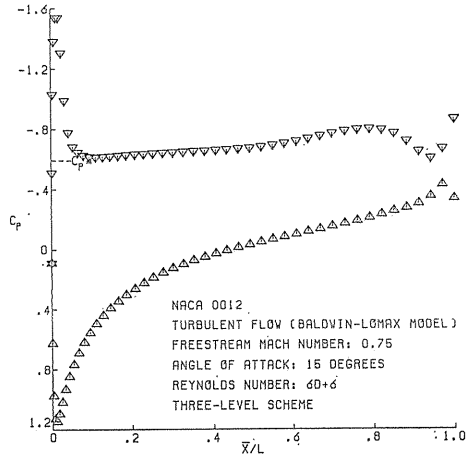

(c) Pressure distribution over the airfoil surface.

Fig. 4. NACA 0012 for $M_\infty=0.75$, $Re=6\times10^6$ and $\alpha=15$ degrees at $N=9000$ steps ($t=51.8$).

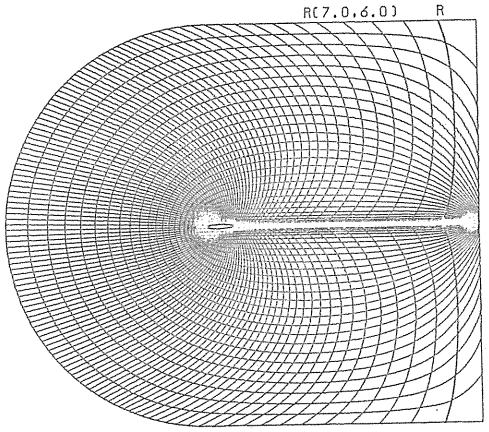

(a) Grid 1.

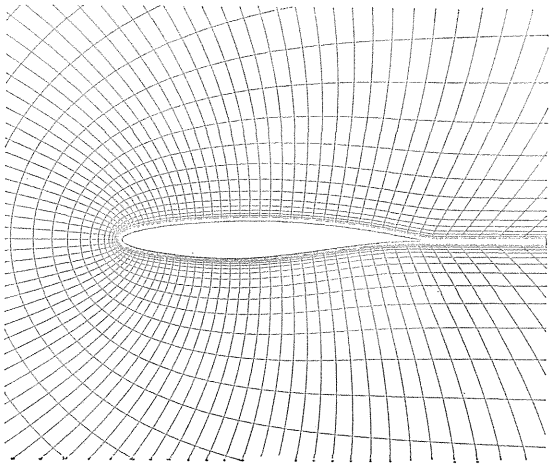

(b) Detailed view of the Grid 1.

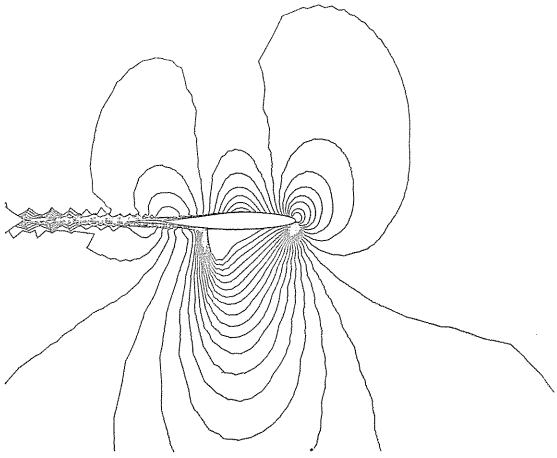

(c) Equi-Mach-number contours.

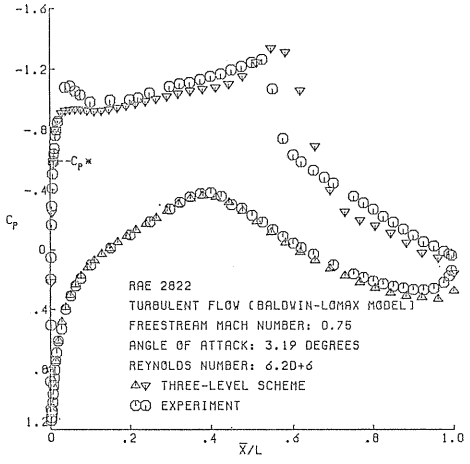

(d) Pressure distribution over the airfoil surface.

Fig. 5. Analysis of flow around the RAE 2822 airfoil for $M_\infty=0.75$, $Re=6.2\times10^6$ and $\alpha=3.19$ degrees at $N=7000$ steps ($t=9.94$).

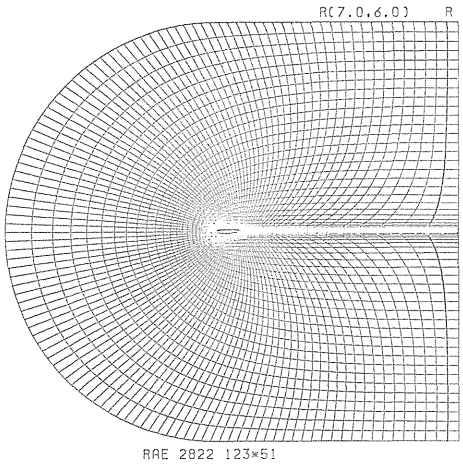

(a) Grid 2.

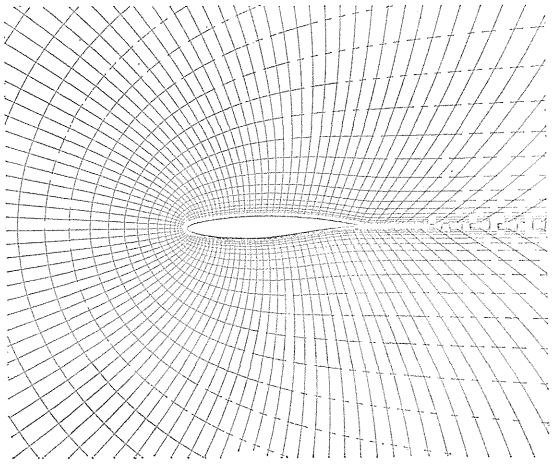

(b) Detailed view of the Grid 2.

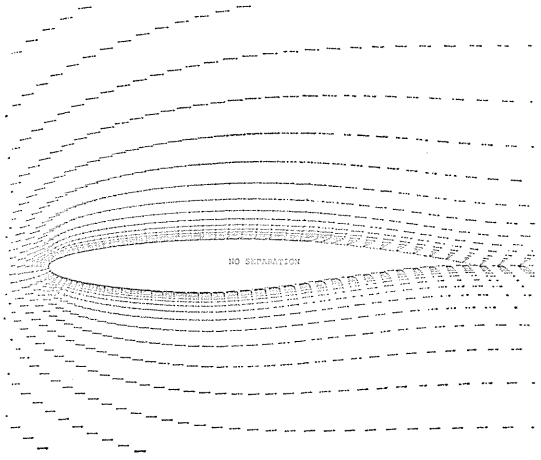

(c) Velocity vectors.

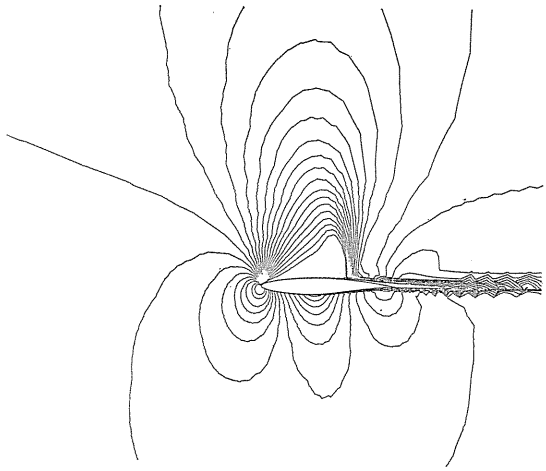

(d) Equi-Mach-number contours.

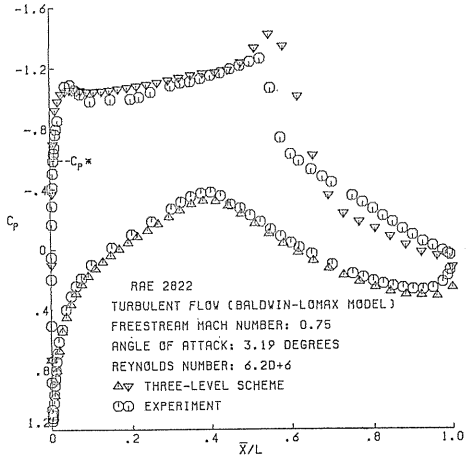

(e) Pressure distribution over the airfoil surface.

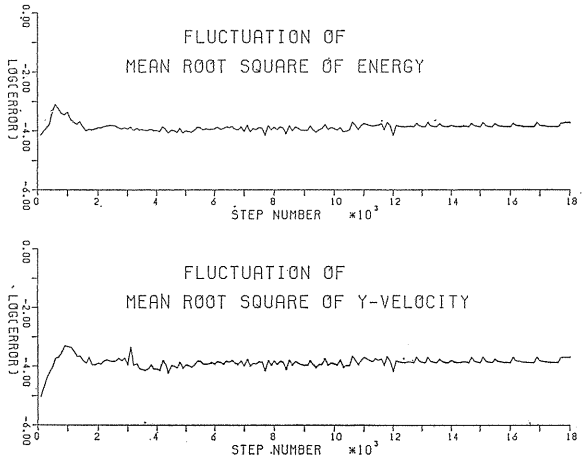

(f) Temporal behaviors of average stepwise variation of physical quantities in the entire field.

Fig. 6. RAE 2822 airfoil for $M_\infty=0.75$, $Re=6.2\times10^6$ and $\alpha=3.19$ degrees at $N=18000$ steps ($t=26.7$).